




Structural, diffuse reflectance and luminescence study of t - $\text{Mg}_2\text{B}_2\text{O}_5$ nanostructures

Jitender Kumar¹ · Rajesh Kumar² · Mukhtiyar Singh² · Shalendra Kumar^{3,6} · Ravi Kumar⁴ · Sung Ok Won⁵ · Ranjeet Brajpuriya⁶ · Sourabh Dwivedi⁷ · Ram K. Sharma⁸ · Ankush Vij⁶ 

Received: 26 March 2021 / Accepted: 13 July 2021 / Published online: 23 July 2021
© The Author(s), under exclusive licence to Springer-Verlag GmbH, DE part of Springer Nature 2021

Abstract

We report here the structural, reflectance, photoluminescence and thermoluminescence study of t - $\text{Mg}_2\text{B}_2\text{O}_5$ nanostructures synthesized using optimized combustion method relatively at much lower temperature. The rietveld refinement of X-ray diffraction data confirms single-phase triclinic crystal structure of $\text{Mg}_2\text{B}_2\text{O}_5$ nanoparticles. The direct band gap determined using diffuse reflectance spectra (DRS) was 5.23 eV, which is contrary to earlier reports quoting $\text{Mg}_2\text{B}_2\text{O}_5$ as indirect band gap material. To elucidate the nature of band gap in $\text{Mg}_2\text{B}_2\text{O}_5$, we performed first principle calculations based on full potential linearized augmented plane-wave (FP-LAPW) method, predicting the direct band gap of 5.10 eV in t - $\text{Mg}_2\text{B}_2\text{O}_5$ which is in good agreement with our experimental results. The t - $\text{Mg}_2\text{B}_2\text{O}_5$ nanoparticles were found to exhibit yellow-reddish photoluminescence peaking at 588 nm, attributed to various defects states. The combustion synthesized $\text{Mg}_2\text{B}_2\text{O}_5$ nanocrystals exhibited ultraviolet (254 nm) responsive thermoluminescence (TL). TL glow curve of $\text{Mg}_2\text{B}_2\text{O}_5$ comprises of one dominant peak around 417–428 K and less intense shoulder around 573–589 K which arouse possibility of various trapping sites or defects present in the sample. The TL analysis using general order Kitti's equations was performed to estimate the activation energies of trapping states. Owing to already well-known mechanical and thermal properties, the direct wide band gap nature and UV responsive thermoluminescence of combustion synthesized t - $\text{Mg}_2\text{B}_2\text{O}_5$ nanostructures can pave way for its use in luminescence-based applications and UV dosimetry. As an additional application of $\text{Mg}_2\text{B}_2\text{O}_5$, anti-biofilms activity of $\text{Mg}_2\text{B}_2\text{O}_5$ nanoparticles using pseudomonas aeruginosa bacterial cells was also performed which revealed $91 \pm 2.7\%$ inhibition of biofilms formed by *P. aeruginosa*, respectively, at 100 $\mu\text{g}/\text{ml}$ after 24 h of treatment.

Keywords t - $\text{Mg}_2\text{B}_2\text{O}_5$ Nanostructures · Photoluminescence · Diffuse reflectance · Thermoluminescence · UV dosimetry

✉ Shalendra Kumar
shailuphy@gmail.com

✉ Ankush Vij
vij_anx@yahoo.com

¹ Nanophosphors Lab, Department of Physics, Amity University Haryana, Gurgaon 122413, India

² Department of Physics, Delhi Technological University, Delhi 110042, India

³ Department of Physics, College of Science, King Faisal University, Hofuf, Al-Ahsa 31982, Saudi Arabia

⁴ Centre for Material Science and Engineering, National Institute of Technology, Hamirpur, Himachal Pradesh 177005, India

⁵ Advance Analysis Centre, Korea Institute of Science and Technology, Seoul 136119, South Korea

⁶ Department of Physics, University of Petroleum and Energy Studies, Dehradun, Uttarakhand 248007, India

⁷ Nanobiotechnology Lab, Aligarh Muslim University, Aligarh 202002, India

⁸ Centre For Interdisciplinary Sciences, University of Petroleum and Energy Studies, Dehradun, Uttarakhand 248007, India

1 Introduction

The optical and luminescent materials are extensively used in variety of applications [1–3]. In particular, there is always a quest for developing luminescent materials possessing good mechanical and thermal properties. Among borate family, bulk and nanowires of $\text{Mg}_2\text{B}_2\text{O}_5$ are mechanically and thermally quite stable, and therefore find immense applications in anti-wear, anti-corrosion, scintillator, discharge lamp, reducing friction additives, turbines, aerospace components, deep submergence structure and armor plate in modern engineering field [4–11]. On the other hand, MgB_4O_7 in its pure and doped form has been extensively studied for optical and luminescence-based applications such as thermoluminescence dosimetry [12, 13]. Owing to robust mechanical and thermal properties, it becomes paramount to investigate the viability of $\text{Mg}_2\text{B}_2\text{O}_5$ nanoparticles for optical and luminescence applications, which is severely lacking in literature so far. The single-phase $\text{Mg}_2\text{B}_2\text{O}_5$ pyroborates are generally crystallized on annealing at higher temperatures. Zhu et al. reported monoclinic $\text{Mg}_2\text{B}_2\text{O}_5$ whiskers synthesized using coprecipitation technique at 832°C but on increasing synthesis temperature monoclinic phase is found to be transforming into triclinic phase [5]. Qasarawi et al. reported synthesis of triclinic $\text{Mg}_2\text{B}_2\text{O}_5$ at 1250°C using partial precipitation technique and found that $\text{Mg}_2\text{B}_2\text{O}_5$ has indirect band gap of 4.72 eV [8]. However, earlier Cheng et al. have theoretically shown that $\text{Mg}_2\text{B}_2\text{O}_5$ has direct band gap of 5.44 eV [14]. The nature of band gap is an important factor for any material to be suitable for optical/ luminescence applications. This led us to investigate the nature of band gap in $\text{Mg}_2\text{B}_2\text{O}_5$ nanoparticles using combined diffuse reflectance spectroscopy and first-principle calculations using density functional theory. The luminescence studies in $\text{Mg}_2\text{B}_2\text{O}_5$ pyroborates did not get much attention as compared to MgB_4O_7 borates. There are only few reports in the literature on the luminescence properties of doped $\text{Mg}_2\text{B}_2\text{O}_5$ synthesized at optimum conditions. Oztas et al. reported the synthesis of pure magnesium pyroborate using solution combustion method (SCS) and conventional ceramic process at various stoichiometries. They concluded that SCS is a time saving and much practical method to synthesis single-phase pyroborates without compromising other properties [15]. Kawano et al. reported the effect of Mn^{2+} doping on photoluminescence properties of $\text{Mg}_2\text{B}_2\text{O}_5$ pyroborate system [16]. Awatif et al. also reported photoluminescence study of europium doped monoclinic $\text{Mg}_2\text{B}_2\text{O}_5$ nanophosphors showing transitions related to both Eu^{2+} and Eu^{3+} [17]. We have very recently investigated the luminescence properties of Eu doped triclinic $\text{Mg}_2\text{B}_2\text{O}_5$ nanophosphors exhibiting intra

4f transitions in Eu^{3+} when excited with 325 nm wavelength [18]. However, luminescence in undoped $\text{Mg}_2\text{B}_2\text{O}_5$ nanocrystals is still unexplored. Being wide band gap material, $\text{Mg}_2\text{B}_2\text{O}_5$ is expected to show defects assisted emission in visible region. Therefore in order to get deep insights on defects or trapping states within band gap of $\text{Mg}_2\text{B}_2\text{O}_5$, thermoluminescence of ultraviolet-irradiated samples was also performed for the first time.

Oxide-based nanostructures also exhibit good antibacterial properties. Several findings show the antimicrobial effects of nanostructured MgO against a range of bacteria. Zhu et al. have stated the antimicrobial action of MgO nanoparticles against E. coli bacteria [19]. He et al. also reported the mechanism of antibacterial activity of magnesium oxide nanoparticles against foodborne pathogens [20]. Nanoparticles as an antimicrobial agents help in combating multi-drug resistance bacteria and also providing long-lasting effects with low toxicity as compared to conventional antibiotics. More often bacteria form biofilms and adhere to the surface of the organism, colonize and become resistant to the conventional antibiotics. To combat such bacteria, nanoparticles have proved to be very effective. Owing to robust antimicrobial properties of MgO nanoparticles, we also investigated effectiveness of combustion synthesized $\text{Mg}_2\text{B}_2\text{O}_5$ ($2\text{MgO} \cdot \text{B}_2\text{O}_3$) nanostructures.

In the present study, single-phase triclinic $\text{Mg}_2\text{B}_2\text{O}_5$ nanocrystals were synthesized using combustion method in the presence of urea as fuel. The combustion method has the advantage of completing chemical reaction at a relatively much lower temperature than solid-state method. We employed rietveld refinement of x-ray diffraction (XRD) data to elucidate the crystal structure of $\text{Mg}_2\text{B}_2\text{O}_5$ nanoparticles (NPs). Thermogravimetric and differential scanning calorimetry was performed in order to get insights about the thermal stability of material. The band gap and luminescence studies were investigated through combined diffuse reflectance spectroscopy (DRS), density functional theory (DFT)-based calculations using WEIN2K, photoluminescence spectroscopy and thermoluminescence (TL). The thermoluminescence was performed on ultraviolet (254 nm) irradiated $\text{Mg}_2\text{B}_2\text{O}_5$ nanostructures. Anti-biofilms activity of $\text{Mg}_2\text{B}_2\text{O}_5$ nanoparticles using pseudomonas aeruginosa bacterial cells was performed.

1.1 Experimental details

1.1.1 Procedure for synthesis of $\text{Mg}_2\text{B}_2\text{O}_5$ nanostructures

The $\text{Mg}_2\text{B}_2\text{O}_5$ nanostructures were prepared using solid combustion synthesis technique. The combustion synthesis is a method based on the principle that once a reaction is initiated under heating, an exothermic reaction occurs that becomes self-sustaining within a certain time

interval, resulting in a powder as final product. Combustion technique is preferred over other synthesis techniques because it does not require high temperature and long time for reaction completion unlike some other techniques like solid state reaction and other methods which require high temperature annealing. Generally, metal nitrates as oxidants and fuels like urea, citric acid, glycine, etc., as reducing agents are used in combustion technique. In the present case, magnesium nitrate was mixed in stoichiometric proportion with urea, boric acid and ammonium nitrate. All chemicals used in the synthesis were of analytical grade. The probable chemical reaction is given as



All the reactants were then grounded using agate mortar and pestle and put in a china dish. By calculating total valency of oxidizers and reducing agents, stoichiometric composition of redox reaction was calculated so that oxidizer to fuel ratio is unity ($O/F = 1$). This china dish was then put into muffle furnace, which is kept preheated at 200 °C and after some time temperature was increased to 600 °C. At this temperature, the combustion starts with decomposition of nitrates resulting in release of flames and fumes. The resulting product in china dish becomes dried. After that china dish was put on metal plate for quenching and the powder was grounded using agate mortar and pestle again. This grounded fine powder was then annealed at 400 °C for 30 min [21].

1.1.2 Biofilm formation in A 96-well microplate

Initially, effects of interaction pattern at Mg₂B₂O₅ NPs-bacteria interface are studied by following growth kinetics of *P. aeruginosa* in the absence and the presence of NPs concentrations in the range between 10 and 100 µg/ml. Test organisms were prepared in LB broth taking loop full of bacteria from the specified slant culture and cultured overnight at 37 °C and 200 rpm agitation. The stock solutions were prepared by dispersing NPs in sterilized LB and sonicated for 10 min followed by UV radiation sterilization before use. The reaction mixtures without NPs were taken as controls. Briefly, 20 µL of bacterial cultures were added to the different reaction mixtures prepared in 96-well plate, and the reaction volumes were adjusted by LB broth to a final volume of 300 µL with NPs. Upon addition of the NP, data collection for growth kinetic studies was immediately performed by measuring optical density (O.D.) at 620 nm using plate reader (Thermo scientific Multiskan EX, REF 51,118,170, China) at regular time interval.

1.1.3 Characterization

The Mg₂B₂O₅ nanophosphors produced from combustion method were characterized by using model D-8 advance Bruker (Germany) diffractometer using Cu-K α radiations having energy 8.04 keV and wavelength 1.54 Å. The morphology and selected area electron diffraction pattern were investigated using JEOL/JEM-F200 transmission electron microscope. Thermal analysis of sample was performed on Simultaneous Thermal Analyzer (STA-8000) of Perkin Elmer. DRS spectroscopy of powder sample was performed on Indian make RIMS (RIII India) set up in the range of

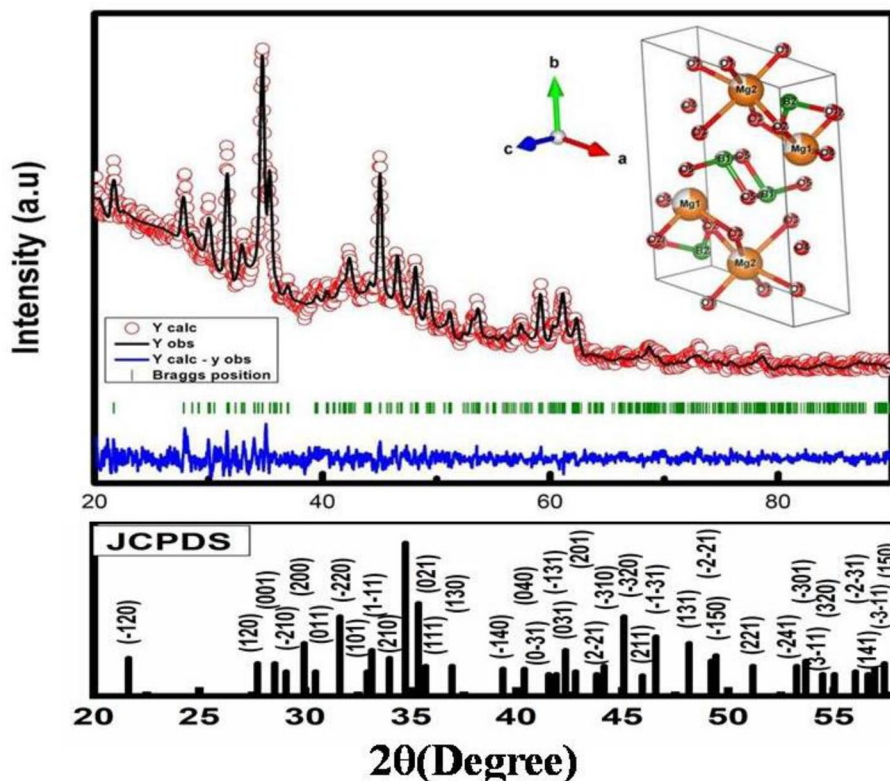
200–700 nm. Photoluminescence was performed on Renishaw In-Via Raman microscope using 325 nm line of He-Cd laser. The UVGL-58 lamp which emits UV radiations of wavelength 254 nm was used to expose the samples at room temperature. One minute of UV exposure at a distance of 3 inch from the sample corresponds to an irradiation of 55.8 mJ/cm². In the present study, the synthesized nanostructures were irradiated with UV radiations of wavelength 254 nm for different interval of times such as 2 min, 5 min, 30 min and 60 min. After the covet exposure, TL curves were recorded on a Harshaw TLD reader (Model 3500). While performing TL experiment, 5 mg of sample is taken for each measurement which is placed in TLD reader under fixed heating rate of 5 K/s.

2 Results and discussion

2.1 Structural analysis

X-ray diffraction is employed to elucidate crystal structure of Mg₂B₂O₅ nanostructures synthesized from combustion method and rietveld refinement was performed using Fullprof software with pseudo-voigt profile shape function which is linear combination of Lorentzian and Gaussian functions with same FWHM (full wavelength at half maximum). Single phase of triclinic Mg₂B₂O₅ nanostructures is confirmed by refinement as shown in Fig. 1. The inset in Fig. 1 also shows the crystal structure of triclinic polymorph of Mg₂B₂O₅. Reliability factors (R) judging the quality of fit are profile R-factor (Rp), weighted profile R-factor (Rwp) and expected R-factor (Rexp) are 3.77, 4.76 and 3.55, respectively, with convergence indicators like chi-square value 1.79 and goodness of fit 1.3, which indicates the validity of refinement [22, 23]. Each Mg is surrounded by six oxygen atoms octahedrally as can also be seen from inset of Fig. 1. Mg₂B₂O₅ nanophosphors is generally known

Fig. 1 Rietveld refined XRD pattern of $\text{Mg}_2\text{B}_2\text{O}_5$ nanostructures and inset shows crystal structure obtained after rietveld refinement



as magnesium pyroborate in which both boron atoms are connected with three oxygen atoms triangularly and there are two such triangular boron atoms with one oxygen in common. Atomic positions of various elements of compound shown in Table 1 are obtained from rietveld refinement. Unit cell parameters which belongs to space group $P-1$ were also determined from rietveld refinement; $a=6.1648$, $b=9.2355$, $c=3.1314$, $\alpha=90.51$, $\beta=92.17$, $\gamma=104.48$. Whereas the parameters obtained by Fan et al. [24] for the similar system synthesized with different technique at 1100°C were; $a=6.1563$, $b=9.2228$, $c=3.1217$, $\alpha=90.46$, $\beta=92.16$, $\gamma=104.39$. The minor difference between these parameters may be due to variation of synthesis conditions which affects crystal structure of material. Rietveld refinement results show the presence of oxygen and magnesium vacancies in the compound while studying occupancy of atoms in $\text{Mg}_2\text{B}_2\text{O}_5$.

2.2 Microscopic analysis

We performed transmission electron microscopy (TEM) to investigate the morphology and particle size of combustion synthesized $t\text{-Mg}_2\text{B}_2\text{O}_5$ nanocrystals. As shown in Fig. 2, TEM images of sample reveal the agglomerated non-uniform sized nanocrystals in the range of 80–110 nm with slightly elongated morphology. High resolution TEM image of sample as shown in Fig. 2 exhibits lattice planes

corresponding to (0,-2,1) plane. The selected area electron diffraction (SAED) pattern has also been shown and d-spacing calculated from SAED pattern belongs to (150) and (1-21) planes of triclinic $\text{Mg}_2\text{B}_2\text{O}_5$. The x-ray diffraction and SAED both confirm the formation of triclinic phase of $\text{Mg}_2\text{B}_2\text{O}_5$ nanocrystals.

2.3 TGA–DSC of $\text{Mg}_2\text{B}_2\text{O}_5$ nanostructures

TGA curve between weight % and temperature for $\text{Mg}_2\text{B}_2\text{O}_5$ is shown in Fig. 3. It is observed that weight % of $\text{Mg}_2\text{B}_2\text{O}_5$ nanophosphors decreases rapidly from 50°C to 226°C , i.e., around 8.54% of weight (2.18 mol of crystal water) is lost. On increasing the temperature, change in weight loss % is around 3.34% in the temperature range from 226°C to 600°C . Further, only 1% weight is lost on raising temperature from 600°C to 800°C . These results show that combustion synthesized $t\text{-Mg}_2\text{B}_2\text{O}_5$ nanostructures are more immune to thermal decomposition i.e., thermally stable. In earlier published papers, researcher got more weight % loss during TGA analysis as compared with current scenario [10], i.e., combustion technique is performed under optimum conditions for synthesis of $\text{Mg}_2\text{B}_2\text{O}_5$ nanophosphors in present study. DSC curve between heat flow and temperature is shown in Fig. 3 which is used for examination of transformation steps and their respective transformation enthalpies at various temperatures. These DSC-TGA experiments were

Fig. 2 **a** TEM **b** Magnified TEM **c** HR-TEM and **d** SAED image of Mg₂B₂O₅ nanostructures

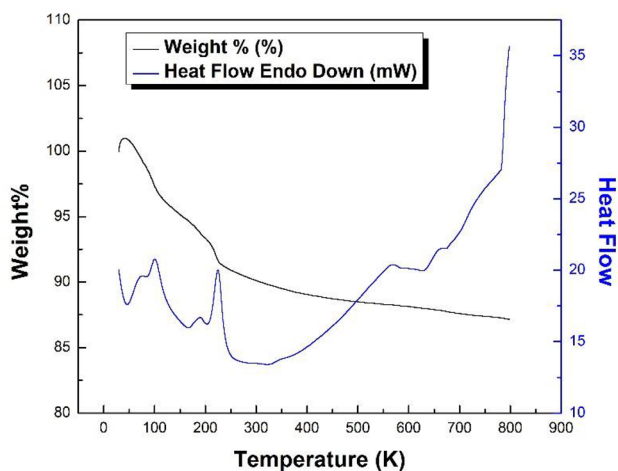
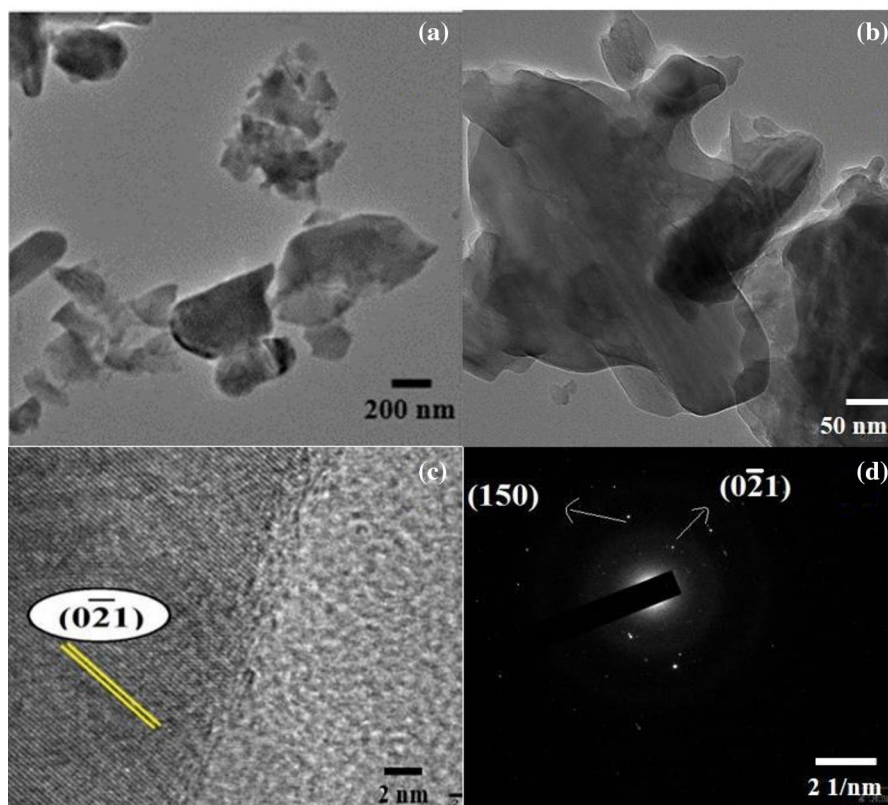


Fig. 3 TG-DSC curves for Mg₂B₂O₅ nanostructures

performed at 2 bar pressure of nitrogen gas at heating rate of 20°C. Here, it is observed that till 600°C mainly three events take place, the first one being an exothermic event with peak temperature 45.86 °C and enthalpy change of -26.8901 J/g (-ve sign for exothermic). The second event is an endothermic with peak temperature 102.12 °C and enthalpy change 14.3939 J/g, while third event is also endothermic with peak temperature at 225.05 °C and has maximum enthalpy change 62.954 J/g. It can be noticed that the endothermic events are

observed at temperatures where material is losing its weight which means it is the process where moisture is getting out. From 226°C to 600°C, there is not as much change in weight % of the sample as well as no phase change is observed in this range, so it is in agreement with structural properties that single-phase triclinic Mg₂B₂O₅ nanophosphor is synthesized under optimum conditions.

2.3.1 Diffuse reflectance spectroscopy

Figure 4a shows the diffuse reflectance spectrum of *t*-Mg₂B₂O₅ nanocrystals, which shows band edge absorption around 250 nm and a broad absorption in the range 300–340 nm. The band edge absorption corresponds to band gap, while broad absorption around 300–340 may be ascribed to absorption in defect states such as oxygen and magnesium vacancies within the band gap as predicted by rietveld refinement analysis. We used Kubelka–munk function to convert reflectance into absorbance to be used in determination of band gap [3, 8]. Kubelka–munk function which is used to express intensity of diffused reflectance spectrum is as follows

$$\frac{k}{s} = \frac{(1 - R_{\infty})}{2R_1} = f(R_1)$$

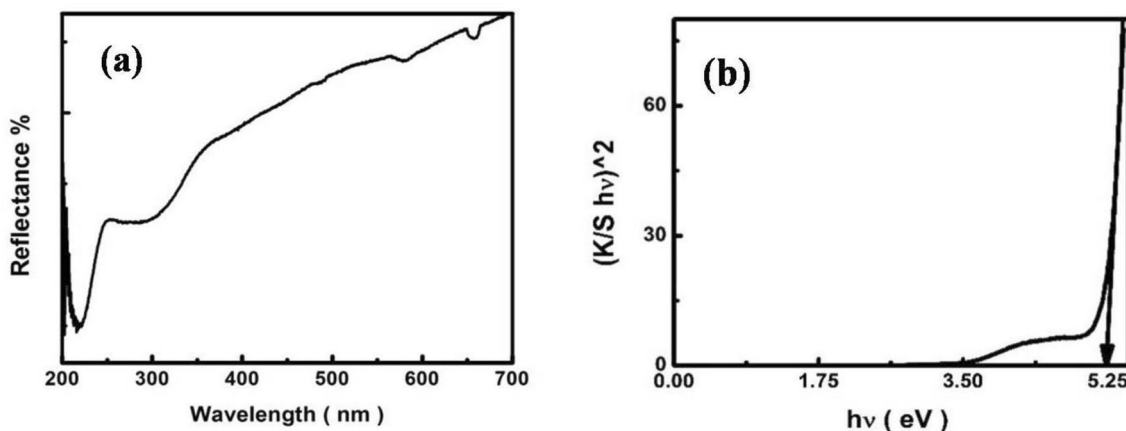


Fig. 4 **a** Diffuse reflectance spectrum of $\text{Mg}_2\text{B}_2\text{O}_5$ nanostructures and **b** Tauc's plot for band gap determination

where K is absorption coefficient, S is scattering coefficient and R_1 absolute diffuse reflectance Tauc's plot, shown in Fig. 4b, reveals direct band gap of 5.23 eV for $t\text{-Mg}_2\text{B}_2\text{O}_5$ nanoparticles. On the other hand, Qasrawi et al. [8] have reported indirect band gap of 4.72 eV in $t\text{-Mg}_2\text{B}_2\text{O}_5$ particles which were synthesized using partial precipitation technique and annealed at very high temperature. Due to lack of available literature, it was crucial to investigate the electronic band structure of $t\text{-Mg}_2\text{B}_2\text{O}_5$ nanoparticles to probe the nature of band gap.

2.3.2 Theoretical estimation of band gap

The electronic structure was calculated using density functional theory (DFT)-based Full Potential Linearized Augmented Plane-Wave (FP-LAPW) method as implemented in WIEN2k program package [25]. In full potential calculations, the core states were treated fully relativistically, whereas for the valence states, a scalar relativistic approximation was used. Generalized gradient approximation (GGA) within the parameterization of Perdew-Burke-Ernzerhof was used to treat the exchange and correlation potential [26]. The radii of muffin-tin (RMT) spheres for various atoms were used in the present calculation to ensure the nearly touching spheres. Plane wave cut-off parameters were decided by $\text{RMTKmax} = 7$ (where K_{max} is the largest wave vector of the basis set). A $9 \times 6 \times 17$ k-points mesh was used as the base for the integration in triclinic system which results in 460 k-points in the irreducible Brillouin Zone (IBZ). The energy convergence criterion was set to 0.0001 Ry/cell and charge convergence was also monitored accordingly.

DFT-based calculations were employed by using the experimentally determined lattice parameters to elucidate band structure of $t\text{-Mg}_2\text{B}_2\text{O}_5$ nanoparticles. The total density of states (TDOS) and the band structure of the system under investigation are shown in Fig. 5a. The system is a

non-magnetic semiconductor with a direct band-gap along $\Gamma\text{-}\Gamma$ direction. The calculated value of energy band-gap is 5.10 eV which is in good agreement with our experimental result. The slightly lower value of band gap is expected using GGA method. The TDOS of this system is mainly governed by O-atoms. Further, to have deep insight of the qualitative features of the DOS, partial (atom-resolved) DOS of $\text{Mg}_2\text{B}_2\text{O}_5$ is also explored (Fig. 5b). It is clear that, except a deep-lying band (from ~ -8.4 eV to ~ -8.15 eV) having major contribution from B- p states, the valence band is dominated by O- p states with a small contribution from B- p states and even smaller from Mg- p states. The conduction band is composed predominantly of p states of O and B atoms.

2.4 Photoluminescence spectroscopy

The direct band gap nature prompted us to investigate photoluminescence (PL) of $t\text{-Mg}_2\text{B}_2\text{O}_5$ nanoparticles. Figure 6a shows the PL spectrum collected at an excitation wavelength of 325 nm using He-Cd laser. PL spectrum comprises of asymmetric broad peak with maxima at 588 nm, which may be ascribed to defects emission related to absorption in magnesium and oxygen vacancies within band gap of $\text{Mg}_2\text{B}_2\text{O}_5$ as predicted by rietveld analysis. Further spectroscopic investigations may be required to comment precise form of defects leading to emission in this system. Figure 6b also shows CIE diagram, depicting overall emission of $t\text{-Mg}_2\text{B}_2\text{O}_5$ in yellow-reddish region of visible region. CRI of sample is found to be 86 with x and y coordinates 0.44 and 0.043, respectively. Already well known for its mechanical and thermal properties, we have demonstrated here that $t\text{-Mg}_2\text{B}_2\text{O}_5$ nanoparticles being direct band-gap may further be tuned with suitable dopants and can be exploited in various luminescence-based applications.

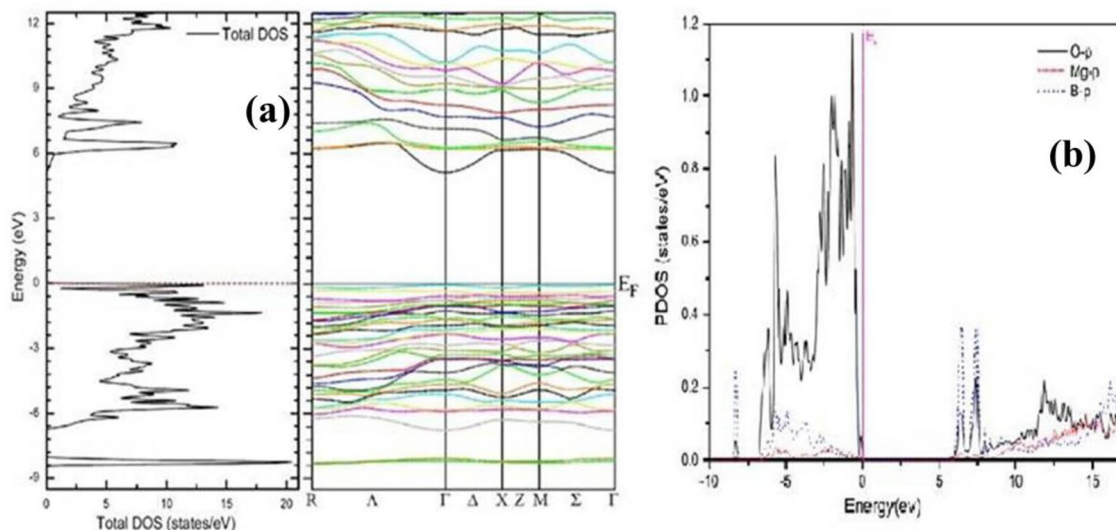


Fig. 5 **a** Total DOS and band structure of Mg₂B₂O₅. Fermi level (E_F) is shifted to 0 Ev. **b** calculated partial DOS of Mg₂B₂O₅

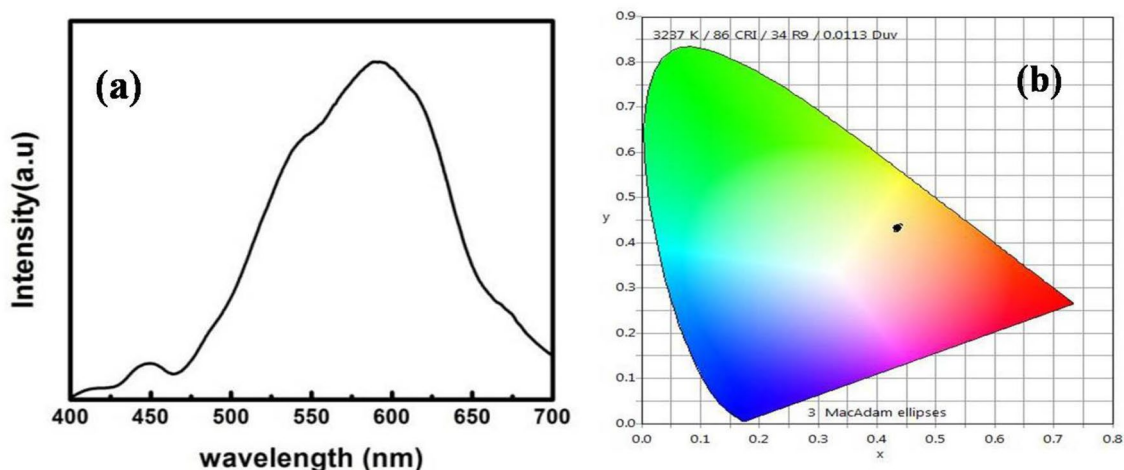


Fig. 6 **a** Photoluminescence emission spectrum of Mg₂B₂O₅ **b** CIE diagram of PL emission

2.5 Thermoluminescence analysis of Mg₂B₂O₅ nanophosphors

TL glow curve of UV (254 nm) irradiated Mg₂B₂O₅ nanostructures is shown in Fig. 7a. TL glow curve of Mg₂B₂O₅ nanostructures comprises of one prominent peak around 417–428 K and a shoulder around 573–589 K. TL signal, as a result of detrapping of trapped carriers in defect states due to increase in temperature which were filled upon UV irradiation, suggests that there may be two kinds of trapping or defect sites present in Mg₂B₂O₅. TL glow curve for 2 min UV exposure shows that the first TL peak dominates over the second one. On increasing UV exposure time, intensity of the first TL peak decreases but there is not much of change in TL intensity of second peak as can

be seen for UV exposure time of 5 and 30 min in Fig. 7b. On further increasing UV irradiation for 60 min exposure time, TL intensity of both peaks decreases. i.e., distribution of trapping sites is immensely affected by UV exposure time. Maximum TL intensity for first peak was found for 2 min UV exposure and maximum TL intensity for second peak was found for 30 min UV exposure. Figure 7b shows that intensity of low-temperature TL peak decreases with UV exposure time consistently, while second TL peak shows abrupt behavior.

Further to get deep insight on the kinetic parameters such as activation energy, order of kinetics and frequency factor, we deconvoluted TL glow curves by TLanal software using Kiti's general order equation [27, 28] given as

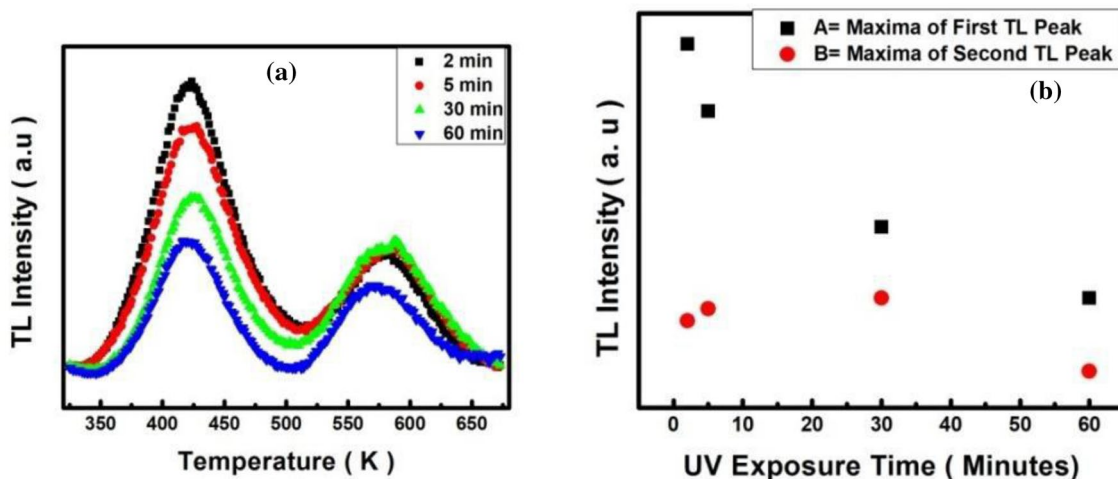


Fig. 7 a TL glow curve of Mg₂B₂O₅ nanostructures exposed to ultraviolet rays of wavelength 254 nm and b TL intensity Vs UV exposure time for both TL peaks

$$I(T) = sn_0 \exp\left(\frac{E}{KT}\right) \left[1 + (b-1) \frac{s}{\beta} \exp \int \left(-\frac{E}{KT'}\right) dT'\right]^{-b(b-1)}$$

where $I(T)$ = Glow Peak Intensity, E = Activation energy, s^{-1} = Frequency factor, n_0 = Initial concentration of trapped charges in cm^{-1} , K = Boltzmann constant, T = Absolute temperature in Kelvin, β = Heating rate, b = Kinetics order.

Figure 8 shows the deconvoluted TL curves of UV irradiated sample for different exposure time. The evaluated trapping parameters of Mg₂B₂O₅ nanophosphors exposed to UV radiation for different times are tabulated in Table 2. It is clear that TL kinetics study of the sample shows the presence of closely lying four kinds of trapping states within the band gap of sample and their distribution changes with change in UV exposure time. The present

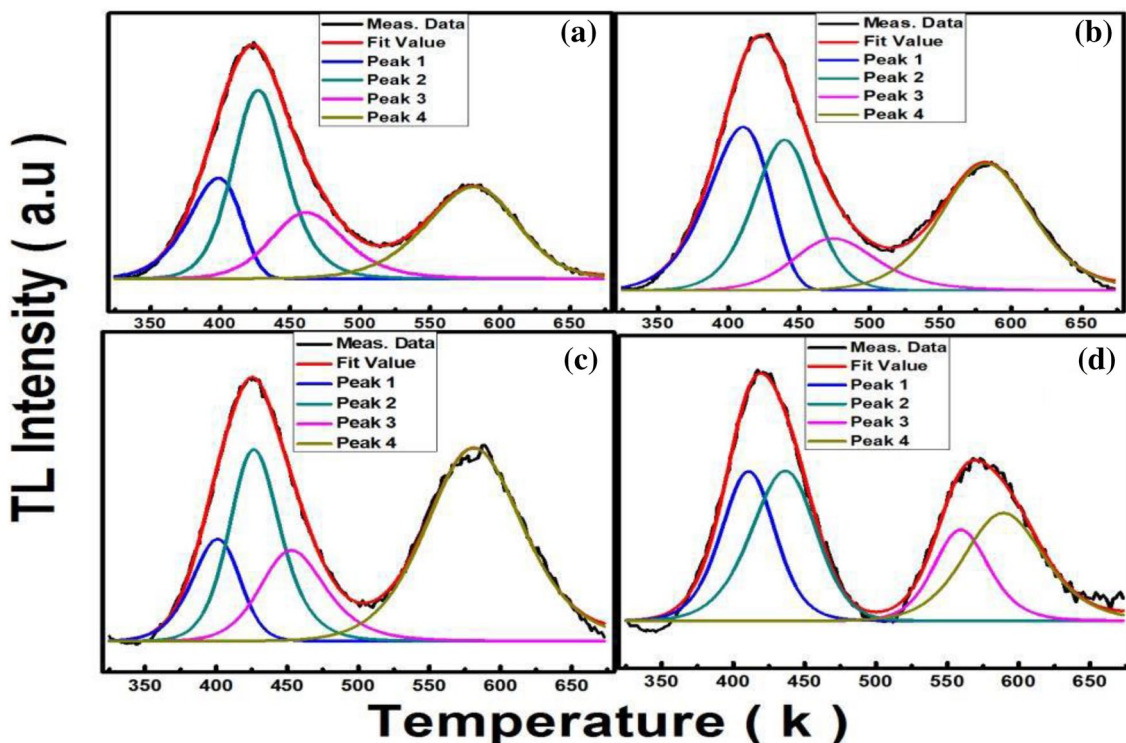


Fig. 8 Deconvoluted TL curves for (a) 2 min (b) 5 min (c) 30 min and (d) 60 min exposure time of UV rays

Table 1 Atomic position and occupancy inferred from rietveld analysis

Atoms	X	Y	Z	Occupancy
O1	0.73235	0.06127	0.26233	0.66677
Mg2	0.37146	0.10007	0.29468	0.77147
B2	1.00987	0.07195	0.18060	1.00
B1	0.52318	0.41301	1.19064	0.82307
O5	0.60357	0.44719	0.71681	0.79247
Mg1	0.16671	0.33051	0.71593	0.70485
O3	0.50637	0.27555	0.75209	0.92353
O4	0.88694	0.28083	0.50265	0.79360
O2	0.09961	0.19603	0.21127	0.80015

study establishes that Mg₂B₂O₅ has trapping states giving rise highly UV responsive TL behavior which can be optimized for TL-based UV dosimetry.

2.6 Antibacterial and antibiofilm activity of nanostructures

Due to increase in drug resistance of pathogens to routinely used antibiotics, it is obligatory to find new and biocompatible antibacterial compounds. For this purpose, combustion synthesized *t*-Mg₂B₂O₅ nanostructures were examined for their antibiofilm activity against *P. aeruginosa*. The results of well diffusion assay on the effect of nanostructures at a dose of 10–100 µl each on the *P. Aeruginosa*. These results were further validated by measuring inhibition of bacterial growth kinetics based on OD620 measurement in a concentration range of 10–100 µg/ml of nanostructures. The data exhibit the dose dependent effect of nanostructures on the test strains in concentration range of 10–100 µg/ml and suggests maximum cytotoxic effect with 100 µg/ml of nanostructures. The results in (Fig. 9) show the nanostructures concentration-dependent inhibition of biofilm formation. The data revealed 91 ± 2.7% inhibition of biofilms formed by *P. aeruginosa*, respectively, at 100 µg/ml after 24 h of treatment. They are regarded as causative agents of many infections in humans. The previous results consistent of this study also reported the antibacterial activity of magnesium oxide nanoparticles alone or in combination with other antimicrobials agents [29]. The mechanism of action of nanoparticles depends on their binding with bacterial surface as well as metabolism in the organism [30, 31]. The present results establish the antibacterial activity as an additional application of *t*-Mg₂B₂O₅ nanostructures which can further be optimized.

Table 2 Kinetic parameters of Mg₂B₂O₅ nanophosphors obtained after deconvolution using TLanal software

Exposure Time	Traps			
	1st Trap	2nd Trap	3rd Trap	4th Trap
2 min				
Energy(eV)	0.71	1.17	0.97	1.03
S''	3.1 × 10 ⁸	2.5 × 10 ¹³	1.2 × 10 ¹⁰	1.6 × 10 ⁸
b	1.0	2	2	1.4
5 min				
Energy(eV)	0.65	0.96	0.91	1.10
S''	2.2 × 10 ⁷	2.8 × 10 ¹⁰	1.1 × 10 ⁹	1.8 × 10 ⁹
b	1.0	1.5	2	1.7
30 min				
Energy(eV)	0.95	1.26	1.11	1.12
S''	3.0 × 10 ¹¹	3.7 × 10 ¹⁴	6.8 × 10 ¹¹	8.9 × 10 ¹⁸
b	1.4	2.0	2.0	1.8
60 min				
Energy(eV)	0.97	0.84	1.99	1.46
S''	3.2 × 10 ¹¹	1.3 × 10 ⁹	2.8 × 10 ¹⁷	6.6 × 10 ¹¹
b	1.6	1.4	2.0	1.9

3 Conclusions

We have successfully synthesized single phase *t*-Mg₂B₂O₅ nanostructures using combustion method at relatively low temperature and optimum synthesis conditions are also supported by TGA–DSC analysis. HR-TEM and SAED images provided confirmation of triclinic phase from d-spacing corresponding to planes of triclinic structure. Experimentally calculated direct band gap (5.2 eV) from diffuse reflectance spectroscopy was found to be in good agreement with DFT calculations. The *t*-Mg₂B₂O₅ nanostructures exhibited

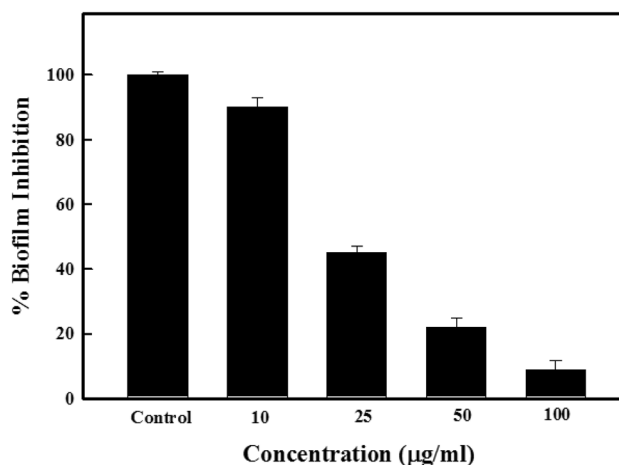


Fig. 9 Concentration dependent inhibition of bacterial biofilm. These data represent the mean ± SD of two independent experiments done in triplicate

defects assisted PL emission in yellow-reddish region. TL kinetics analysis of UV irradiated samples shows the presence of four closely lying trapping sites and their distribution changes with UV exposure time. The present study confirms the direct band gap nature of $\text{Mg}_2\text{B}_2\text{O}_5$ nanostructures and these samples can be further optimized by adding suitable dopants for various luminescence-based applications and TL-based UV dosimetry. It has also been found that *t*- $\text{Mg}_2\text{B}_2\text{O}_5$ nanostructures show good antibacterial properties.

Acknowledgements A Vij is thankful to UGC-DAE Consortium for Scientific Research for financial support through project CSR-IC-BL-74/CRS-191/2016-17/855. Thanks are due to the Director, IUAC New Delhi for allowing us to perform and Mr Beerender Singh for helping in TL experiments at Health Physics Lab. The authors would also like to acknowledge the support provided under the DST-FIST Grant No.SR/FST/PS-I/2019/68 of Govt. of India to Amity School of Applied Sciences, Amity University Haryana.

Declarations

Conflict of interest The authors declare that they have no known competing financial interests or personal relationships that could have appeared to influence the work reported in this paper.

References

- M. Jain, A. Gundimeda, S. Kumar, G. Gupta, S.O. Won, K.H. Chae, A. Vij, A. Thakur, *Appl. Surf. Sci.* **480**, 945–950 (2019)
- Manju, M. Jain, P. Vashishtha, S. Kumar, P. Rajput, G. Gupta, A. Vij, A. Thakur, *J. Mater. Chem. C* **8**, 3147–3155 (2020)
- A. Vij, S. Kumar, S.O. Won, K.H. Chae, A. Dubey, R. Kumar, *Mater. Lett.* **227**, 169–171 (2018)
- S. Li, X. Fang, J. Leng, H. Shen, Y. Fan, D. Xu, *Mater. Lett.* **64**, 151–153 (2010)
- D. Zhu, X. Nai, C. Zhu, F. Guo, S. Bian, W. Li, *Internat. J. Minerals Metallurgy Mater.* **19**, 969–972 (2012)
- X. Tao, X. Li, *Catalyst-Free Synthesis. Nano Lett.* **8**, 505–510 (2008)
- Y. Li, Z. Fan, J.G. Lu, R.P.H. Chang, *Chem. Mater.* **16**, 2512–2514 (2004)
- A.F. Qasrawi, T.S. Kayed, A. Mergen, M. Guru, *Mater. Res. Bull.* **40**, 583–589 (2005)
- S. Li, D. Xu, H. Shen, J. Zhou, Y. Fan, *Mater. Res. Bull.* **47**, 3650–3653 (2012)
- U. Dosler, M.M. Krzmann, D. Suvorov, *J. Euro. Ceram. Soc.* **30**, 413–418 (2010)
- A. Ucyildiz, I. Girgin, *Central Europ. J. Chem.* **8**(4), 758–764 (2010)
- P.D. Sahare, M. Singh, P. Kumar, *J. Lumin.* **160**, 158–164 (2015)
- E.G. Yukihara, E.D. Milliken, B.A. Doull, *J. Lumin.* **154**, 251–259 (2014)
- W. Cheng, H. Zhang, F. Zheng, J. Chen, Q. Zhang, R. Pandey, *Chem. Mater.* **12**, 3591–3594 (2000)
- N.A. Oztas, H. Erdogan, *Zeitschrift für Anorganische und Allgemeine Chemie* **635**, 1626–1632 (2009)
- T. Kawano, T. Suehiro, T. Sato, H. Yamane, *Preparation. J. Lumin.* **130**, 2161–2165 (2010)
- A.B. Awatif, E.M. Elssfah, *Elixir Nanotechnology* **75**, 27521–27524 (2014)
- J. Kumar, A. Sharma, S.O. Won, R. Kumar, K.H. Chae, S. Kumar, A. Vij, *Vacuum* **180**, 109602 (2020)
- X. Zhu, D. Wu, W. Wang, F. Tan, P.K. Wong, X. Wang, X. Qiu, X. Qiao, *J. Alloys Comp.* **684**, 282–290 (2016)
- Y. He, S. Ingudam, S. Reed, A. Gehring, T.P. Strobaugh, P. Irwin, *J. Nanobiotech.* **14**(1), 54 (2016)
- J. Kumar, A. Yadav, P.A. Alvi, S. Kumar, A. Vij, *AIP Conference Proceedings* **2093**, 020025 (2019)
- M. Tsubota, J. Kitagawa, *Sci. Rep.* **7**(1), 15381 (2017)
- B.H. Toby, *Powder Diffr.* **21**(1), 67–70 (2006)
- G. Fan, H. Zhou, X. Chen, *J. Mater Sci: Mater. Electron.* **28**, 818–822 (2017)
- P. Blaha, K. Schwarz, G.K.H. Madsen, D. Kvasnicka, J. Luitz, *WIEN2k, An Augmented Plane Wave Plus Local Orbitals Program For Calculating Crystal Properties* (Viana Univ. of Tech, Austria, 2001)
- P. Perdew, K. Burke, M. Ernzerhof, *Phys. Rev. Lett.* **77**, 3865 (1996)
- C. Furetta, G. Kitis, P.S. Weng, T.C. Chu, *Nucl. Instrum. Methods Phys. Res. A* **420**, 441–445 (1999)
- G. Kitis, V. Pagonis, *Nucl. Instrum. Methods Phys. Res. B* **262**, 313–322 (2007)
- A. Arshad, J. Iqbal, M. Siddiq et al., *J. Appl. Phys.* **121**(2), 024901 (2017)
- L. Castro, M. L. Blázquez, J. á. Muñoz, F. G. González, A. Ballester, *Rev. Adv. Sciences Eng.* **3**(3), 199–216 (2014)
- L. Wang, C. Hu, L. Shao, *Internat. J. Nanomed.* **12**, 1227–1249 (2017)

Publisher's Note Springer Nature remains neutral with regard to jurisdictional claims in published maps and institutional affiliations.